JOURNAL OF GEOPHYSICAL RESEARCH, VOL. 114, C12029, doi:10.1029/2009JC005492, 2009

Click Here for Full Article

Geostrophic dynamics of meridional transport variability in the subpolar North Atlantic

R. J. Bingham[1] and C. W. Hughes[2]

Received 5 May 2009; revised 19 August 2009; accepted 9 September 2009; published 31 December 2009.

[1] The North Atlantic meridional overturning circulation (MOC) is believed to play an important role in regulating the Earth's climate. Yet, there is still much uncertainty regarding the dynamics of the MOC and its variability. It is well established, however, that through geostrophy the zonally integrated meridional transport at a particular latitude and depth can be determined from the east-west bottom pressure difference across the basin. Therefore, rather than consider the MOC as a large-scale system, this paper focuses on the dynamics of this geostrophic relationship in two numerical ocean models at a single latitude (50°N) in the subpolar Atlantic. First, it is shown that the bottom pressure on the western boundary is sufficient to recover, with high fidelity, the interannual meridional transport variability at 50°N over a 100 year period in the climate model HadCM3. It is found that the variability of western boundary pressure is closely associated with density changes over the continental slope. These changes lead to a large zonal gradient in potential energy and imply an unfeasible depth-mean velocity over the slope. The western boundary pressure, from which the meridional transport can be recovered, is generated as a compensation to this and limits the depth-mean flow. This demonstrates that in numerical ocean models, at least, meridional transport variability is generated as a local response to density changes on the western slope. Whether this is a true representation of actual ocean variability is uncertain, but if it were, then meridional transport variability could largely be determined using only the density field on the western slope.

Citation: Bingham, R. J., and C. W. Hughes (2009), Geostrophic dynamics of meridional transport variability in the subpolar North Atlantic, *J. Geophys. Res.*, *114*, C12029, doi:10.1029/2009JC005492.

1. Introduction

[2] Much recent interest in the dynamics of the North Atlantic's meridional overturning circulation (MOC) has been stimulated by modeling studies which have suggested that a collapse of the MOC would result in a dramatic change in the Northern Hemisphere climate [*Manabe and Stouffer*, 1999; *Vellinga and Wood*, 2002; *Wood et al.*, 2003]; a concern strengthened by evidence that such changes have occurred in the past [*McManus et al.*, 2004]. Within an ocean model, at least, the time-mean MOC is easily visualized by computing the stream function of the zonally integrated mean transport as a function of depth and latitude (see Figure 1). However, due to a paucity of suitable observations, a similar characterization of the physical MOC is not so easily obtained, but those studies that have been done, seem to confirm, at least qualitatively, the ability of numerical ocean models to reproduce the present, steady state MOC [*Ganachaud and Wunsch*, 2003; *Talley et al.*, 2003].

[3] While there is still much debate concerning the driving force that maintains the steady state of the MOC, it is more certain that deep water formation through convection in the subpolar North Atlantic and Nordic Seas plays a critical role in supplying mass, if not energy, to the overturning circulation (see review paper by *Kuhlbrodt et al.* [2007]). Variability of the MOC has been linked to changes in the rate of deep water formation, with some finding convection in the Labrador Sea of primary importance [*Marsh*, 2000; *Cooper and Gordon*, 2002; *Latif et al.*, 2006], and others finding the Nordic Seas the greater contributor to MOC variability [*Gerdes and Köberle*, 1995; *Koltermann et al.*, 1999; *Köhl and Stammer*, 2008; *Guemas and Salas-Mélia*, 2008; *Deshayes and Frankignoul*, 2008]. In turn, the changes in deep water formation rate through convection have been linked to the North Atlantic Oscillation (NAO) [*Mauritzen and Hakkinen*, 1999; *Hakkinen*, 2001; *Curry and McCartney*, 2001; *Eden and Jung*, 2001; *Eden and Willebrand*, 2001; *Esselborn*, 2001; *Cheng et al.*, 2004], which, in its more vigorous state, deepens the mixed layer and promotes convection through enhanced cooling and mixing. Alternatively, *Mauritzen and Hakkinen* [1999], while also finding a link between the NAO and MOC, propose that this occurs largely through changes in the volume of water classes, due to the entrainment of thermocline waters by the dense overflows at the Greenland-Scotland ridge. There is also some debate as to whether the ocean, and in particular the MOC, responds passively to the NAO or plays an active role as suggested by *Eden and Greatbatch* [2003]. Additionally, *Spall* [2008]

[1]Department of Civil Engineering and Geosciences, Newcastle University, Newcastle upon Tyne, UK.
[2]Proudman Oceanographic Laboratory, Liverpool, UK.

Copyright 2009 by the American Geophysical Union.
0148-0227/09/2009JC005492$09.00

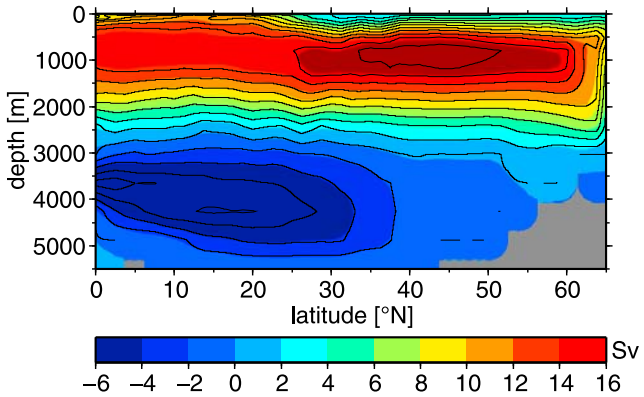

Figure 1. An example of the North Atlantic temporal mean meridional overturning stream function computed from the OCCAM model by zonal integration of velocity fields across the basin.

concludes that low-frequency MOC variability can be generated by many factors other than buoyancy fluxes, including lateral advection, acting on the baroclinic pressure gradient in the mixed layer. Moreover, it has been suggested that MOC variability can be generated internally, with no external atmospheric forcing, through the interaction of horizontal pressure gradients and the ocean circulation [*Zhu and Jungclaus*, 2008].

[4] The MOC is generally conceived of as a large-scale feature of the ocean's circulation, as exemplified by the stream function in Figure 1, and the phrase MOC variability is suggestive of meridionally coherent variability of this large-scale feature. Clearly, due to mass conservation, on some time scale this must be the case. In fact, simple models predict that meridional adjustment to the rate of deep water formation at high latitudes occurs rapidly through southward propagating coastally trapped waves [e.g., *Kawase*, 1987; *Johnson and Marshall*, 2002], supporting the notion of a meridionally coherent entity, at all but the shortest time scales. However, in a range of sophisticated numerical models [*Bingham et al.*, 2007] found that much of the zonally integrated meridional transport variability (henceforth, often abbreviated to transport variability) at any particular latitude is localized and only weakly correlated with the transport variability at other latitudes, even for interannual variability. Furthermore, both *Sime et al.* [2006] and *Cabanes et al.* [2008] describe how the factors driving transport variability are latitudinally dependent. This apparent discrepancy can perhaps be resolved by thinking of the transport variability at any particular latitude as being the sum of a meridionally coherent mode (of the sort evoked by the phrase MOC variability) and locally generated, meridionally incoherent variability.

[5] Because these two components of transport variability are not readily separated, in this study, rather than attempting to explain MOC variability as part of a large-scale system, we shall restrict ourselves to understanding the total transport variability at a single latitude. However, we focus on 50°N, which, from our previous work, appears gives the clearest picture of low-frequency meridionally coherent transport variability [*Bingham et al.*, 2007]. We take as our starting point the geostrophic balance that is known to hold between the zonally integrated meridional transport and the east-west pressure difference across the basin. Confirming a result from our earlier work [*Bingham and Hughes*, 2008] we find that much of the transport variability at 50°N in HadCM3 can be recovered from pressure on the western boundary. Previously, we have used this to show how the MOC could potentially be monitored using measurements from the western boundary. Here, however, our primary objective is to show that it is to the western boundary that we must look if we are to understand the proximate mechanism of transport variability at 50°N. We find that the western boundary pressure arises locally from changes in the density field over the continental slope. Given that 50°N intersects the subpolar gyre, and knowing that deep water formation occurs in the western part of the basin, it is not surprising that we find such density anomalies on the western boundary. However, that these density variations lead to the bottom pressure signal from which we can determine the transport variability is a surprising result.

[6] In section 2 we show how the temporal variability of the meridional transport can be decomposed in such a fashion that its calculation only depends on relative, rather than absolute, sea level. This is important due to difficulties with the diagnosis of sea level from the HadCM3 model. Brief descriptions of the models used are provided in section 3. In section 4 we give a qualitative account of the transport variability at 50°N in HadCM3, followed by a demonstration of the geostrophic calculation and an examination of the fields from which the transport variability is determined. This is supplemented by an examination of the same fields in the higher-resolution Ocean Circulation and Climate Advanced Modelling project (OCCAM) model in section 5. In section 6 we propose a mechanism to explain how density variations lead to the required bottom pressure signal. Finally, in section 7, our results are discussed, and conclusions are provided.

2. Decomposition of the Meridional Transport

[7] According to geostrophy, in the absence of intervening topography, at each latitude the zonal integral of the meridional transport as a function of depth is given by

$$T(z) = \frac{p_e^b(z) - p_w^b(z)}{\rho_0 f_0}, \tag{1}$$

where $p_e^b(z)$ and $p_w^b(z)$ are the bottom pressures on the eastern and western boundaries of the basin, ρ_0 is the mean density of seawater, and f_0 is the Coriolis parameter. (For a more complete justification of equation (1) see *Bingham and Hughes* [2008].) Equation (1) can be used to compute the absolute transport given the absolute pressure field. However, here we are concerned with transport variability, and so it can be assumed that the time mean has been removed from the pressures, and T is the anomalous transport. Here z is positive out of the ocean and $z = 0$ corresponds to position of the time-mean sea surface.

[8] The basin boundaries are, of course, formed by the continental slopes. Because these have finite gradients, over the slopes, quantities, such as sea level and bottom pressure, which are more usually thought of as varying with lateral

position, can also be viewed as dependent on depth. For a zonally dependent field $F(x)$ (we ignore meridional dependence, since we are considering a fixed latitude), we use the notation $F_{e,w}(z) \equiv F(x = x_{e,w}(z))$ to indicate the value of F at the zonal position $x = x_{e,w}(z)$ on the eastern (subscript e) and western (subscript w) boundaries corresponding to depth z.

[9] Equation (1) assumes no intervening topography. Yet, at 50°N the Mid-Atlantic Ridge (MAR) shoals at a depth of 2800 m. Potentially, therefore, at this latitude the geostrophic transport calculation at depths below 2800 m may need to take into account the pressure on the flanks of the MAR, and the transport below 2800 m would then be given by the sum of the pressure difference between the eastern boundary and the eastern flank of the MAR and pressure difference between the western boundary and the western flank of the MAR. However, it will be shown below that neglect of the MAR has no significant effect on the transport calculation at the time scales of interest here. The reasons for this are described by *Bingham and Hughes* [2008].

[10] Assuming hydrostatic balance, the bottom pressure on the boundaries is given by

$$p^b_{e,w}(z) = g\rho_0\left(\eta_{e,w} - \eta^s_{e,w}\right), \tag{2}$$

where $\eta_{e,w}$ is anomalous sea level (relative to the time-mean sea surface) at the eastern and western boundary points, g is the acceleration due to gravity, and

$$\eta^s_{e,w} = -\int_z^0 \rho_{e,w}(z')/\rho_0 dz' \tag{3}$$

is the steric component of the anomalous sea level resulting from the anomalous density field $\rho_{e,w}$ (the absolute density minus its time mean) over the depth of the water column at the boundary points. Substitution into equation (1) leads to

$$T(z) = g\left\{\left(\eta_e - \eta^s_e\right) - \left(\eta_w - \eta^s_w\right)\right\}/f_0. \tag{4}$$

[11] For this analysis it is useful to decompose the meridional transport into a depth-mean component $\overline{T}$ and a depth-dependent component $\hat{T}$, and to further decompose each of these into eastern and western boundary components (although, this does not imply that the actual flow is on either the eastern or western boundary, only that this is where the quantities in the calculation are located). Thus, we have

$$T = \left(\overline{T}_e - \overline{T}_w\right) + \left(\hat{T}_e - \hat{T}_w\right). \tag{5}$$

The depth-mean components are given by

$$\overline{T}_{e,w} = g\left(\overline{\eta}_{e,w} - \overline{\eta}^s_{e,w}\right)/f_0, \tag{6}$$

where

$$\overline{\eta}_{e,w} = \frac{1}{H_{\max}}\int_{-H_{\max}}^0 \eta_{e,w} dz \tag{7}$$

is the depth mean of sea level over the boundary, and similarly for $\overline{\eta}^s_{e,w}$. $H_{\max}$ is the depth at the bottom of the slope. Finally, the depth-dependent components of the meridional transport are given by

$$\hat{T}_{e,w} = g\left(\hat{\eta}_{e,w} - \hat{\eta}^s_{e,w}\right)/f_0 \tag{8}$$

where $\hat{\eta}_{e,w} = \eta_{e,w} - \overline{\eta}_{e,w}$ and similarly for $\hat{\eta}^s_{e,w}$.

[12] As *Bingham and Hughes* [2008] show, the depth-independent component of the meridional transport is dominated by the geostrophic compensation of the Ekman transport. The dynamics of this are relatively well understood, and, in an observational context, this component could be recovered from the wind stress. Therefore, our focus in this paper is the dynamics of the depth-dependent component of the meridional transport. The above derivations show that this does not depend of the absolute value of sea level at either boundary, only on its zonal variation over the lateral ranges spanned by the boundaries. This is important for the present study using HadCM3 since, as described in the appendix, it is only possible to determine the relative value of sea level, not the absolute value, with sufficient accuracy for use in the geostrophic calculation.

3. Models

[13] The results of this paper are based on two quite different numerical models. The first is the Hadley Centre coupled atmosphere-ocean model HadCM3, which simulates a realistic and stable present-day mean climate without the need of unphysical flux adjustments required in many coupled models in order to prevent climate drift [*Gordon et al.*, 2000]. The atmospheric component of HadCM3 has a resolution of 2.5° in latitude and 3.75° in longitude, and has 19 vertical levels. The oceanic component has a horizontal resolution of 1.25° in both latitude and longitude, and has 20 depth levels, which vary in thickness from 10 m near the surface to 500 m at the bottom. Here we examine a 100 year section (years 2079–2178) from a control run of HadCM3 with preindustrial atmospheric conditions. For this run, the model was initialized from the climatology of Levitus [*Levitus et al.*, 1994; *Levitus and Boyer*, 1994], with a spin-up period of 360 years.

[14] The second model is the eddy-permitting Ocean Circulation and Climate Advanced Modeling project model (OCCAM), run at the National Oceanography Centre, Southampton. OCCAM is a z coordinate, global, free surface model with a rotated grid over the North Atlantic, forced with 6 hourly ECMWF atmospheric data. The run we are considering (run 202) is at 0.25° resolution, with 66 vertical levels, over the 19 year period 1985–2003, after 4 years of spin-up [*Coward and de Cuevas*, 2005].

[15] In this study we are concerned with interannual variability. For the analyzed model output, this component has been extracted by removal of the mean seasonal cycle and the application of a 13 month boxcar filter. Henceforth, to save repetition, in all references to variability, it can be assumed that we mean interannual variability.

4. Meridional Transport in HadCM3

4.1. Descriptive Account

[16] We begin with a descriptive account of the zonally integrated meridional transport variability at 50°N in HadCM3.

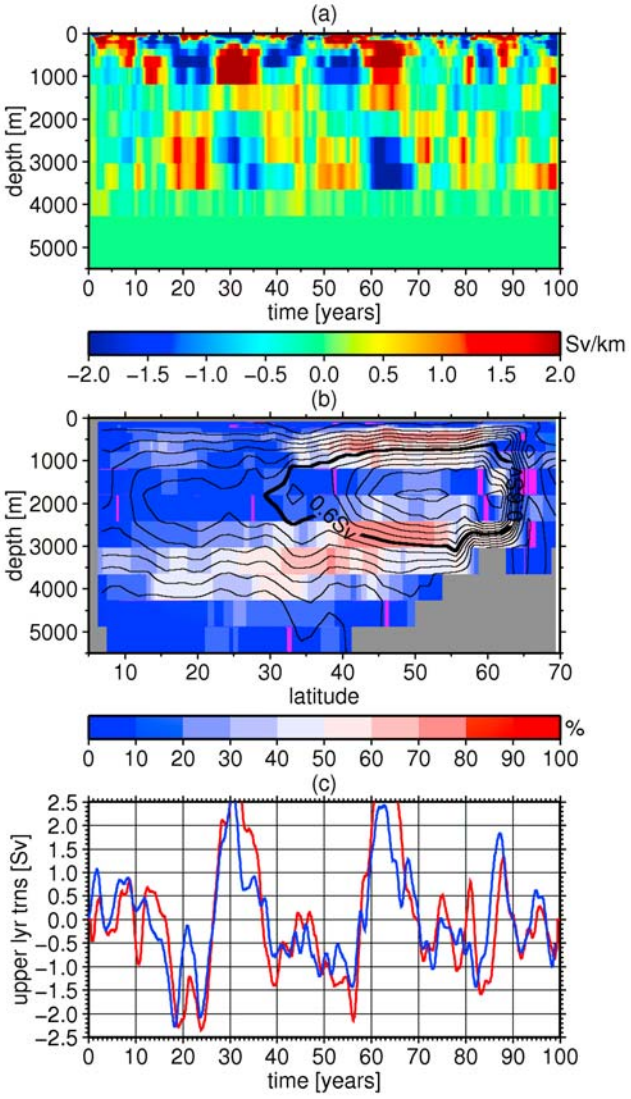

Figure 2. (a) The interannual variability of the zonal integral of meridional transport at 50°N in HadCM3 for the 100 year control run. (The units of Sv/km are used merely as a convenient scaling.) (b) The spatial function of the leading EOF of interannual zonally integrated meridional transport variability in HadCM3 (contour interval is 0.1 Sv). Colors represent the percent of the interannual variance accounted for by the leading EOF at each depth and latitude. (c) The total interannual meridional transport within the depth range 100–1800 m (red) and the temporal function of the leading EOF (blue).

Figure 2a shows that, unlike the time-mean transport (as illustrated in Figure 1), the transport variability cannot be neatly partitioned into discrete opposing layers. However, we can identify two prominent events, roughly between years 20 and 30, and years 55 and 65, where the northward transport increases by several sverdrups above 1800 m, while below there is a corresponding increase in southward transport. We therefore take the integral of the transport over the depth range 100–1800 m (which we shall denote by T_U) as an index of the transport variability at this latitude (Figure 2c, red). This shows that for the two prominent events the increase in transport strength is about 4.5 Sv over a period of 10 years.

[17] To see how the transport variability at 50°N is related to the variability at other latitudes, we calculate normalized empirical orthogonal functions (EOFs) from the zonally integrated meridional transport as a function of latitude and depth. The leading EOF (Figures 2b and 2c, blue) demonstrates that the transport variability at 50°N is part of a larger-scale coherent pattern of variability that extends over the entire meridional extent of the North Atlantic basin. This mode is the dominant component north of about 40°N, explaining a large fraction of the variance in this region. South of 40°N it accounts for much less of the variance above 2000 m (because as *Bingham et al.* [2007] show, higher-frequency variability is greater here). Yet, it remains the dominant feature in the deeper ocean. Note that some of the more short-term fluctuations at 50°N do not appear in the temporal function of EOF1, indicative of their more localized nature. The two prominent events, however, do appear in the temporal function, showing that they reflect large-scale changes in the North Atlantic MOC.

4.2. Geostrophic Calculation

[18] Above we showed how the transport variability can be partitioned into east and west informational components. Here we perform the described calculations using the model data at 50°N. There are two reasons that motivate us in this regard: First, from a practical, observational perspective, it provides some insight regarding successful strategies for monitoring the MOC, the object of ongoing efforts. Secondly, and perhaps more importantly, it points us in the direction we should look if we wish to understand the underlying dynamics of the transport variability. As we see directly below, it is to the western boundary we should look in both regards. Later it will be shown that it is the nature of the density variations on the western slope that are the proximate cause of the western boundary pressure variations from which we can recover much of the transport variability at 50°N.

[19] For the OCCAM model, *Bingham and Hughes* [2008] show that bottom pressure from the western boundary is sufficient to determine the transport variability at 42°N. Figures 3 and 4 show, in much the same way as we did for OCCAM, the results of a similar geostrophic calculation of the transport variability at 50°N in HadCM3. Comparing Figure 3a with the directly integrated transport (Figure 2a) shows that the geostrophic calculation using both east and west boundary pressures is successful in recovering most of the transport variability in HadCM3 at 50°N. This is confirmed in Figure 3b, which shows the difference between the geostrophically and directly computed transports. However, the fact that the residual is nonzero shows the determination is not entirely successful. In part, this is due to the numerics of the calculation, which involve interpolation and finite differences. It is also due to the fact that we have, as discussed above, neglected any pressure differences resulting from the intervening topography. Figure 4a, which shows the depth integral of the meridional transport over the upper layer defined earlier, summarizes the accuracy of the geostrophic calculation. The correlation of the geostrophically computed time series with the directly determined time series, T_U, is 0.91, and accounts for 82% of the total variance in T_U.

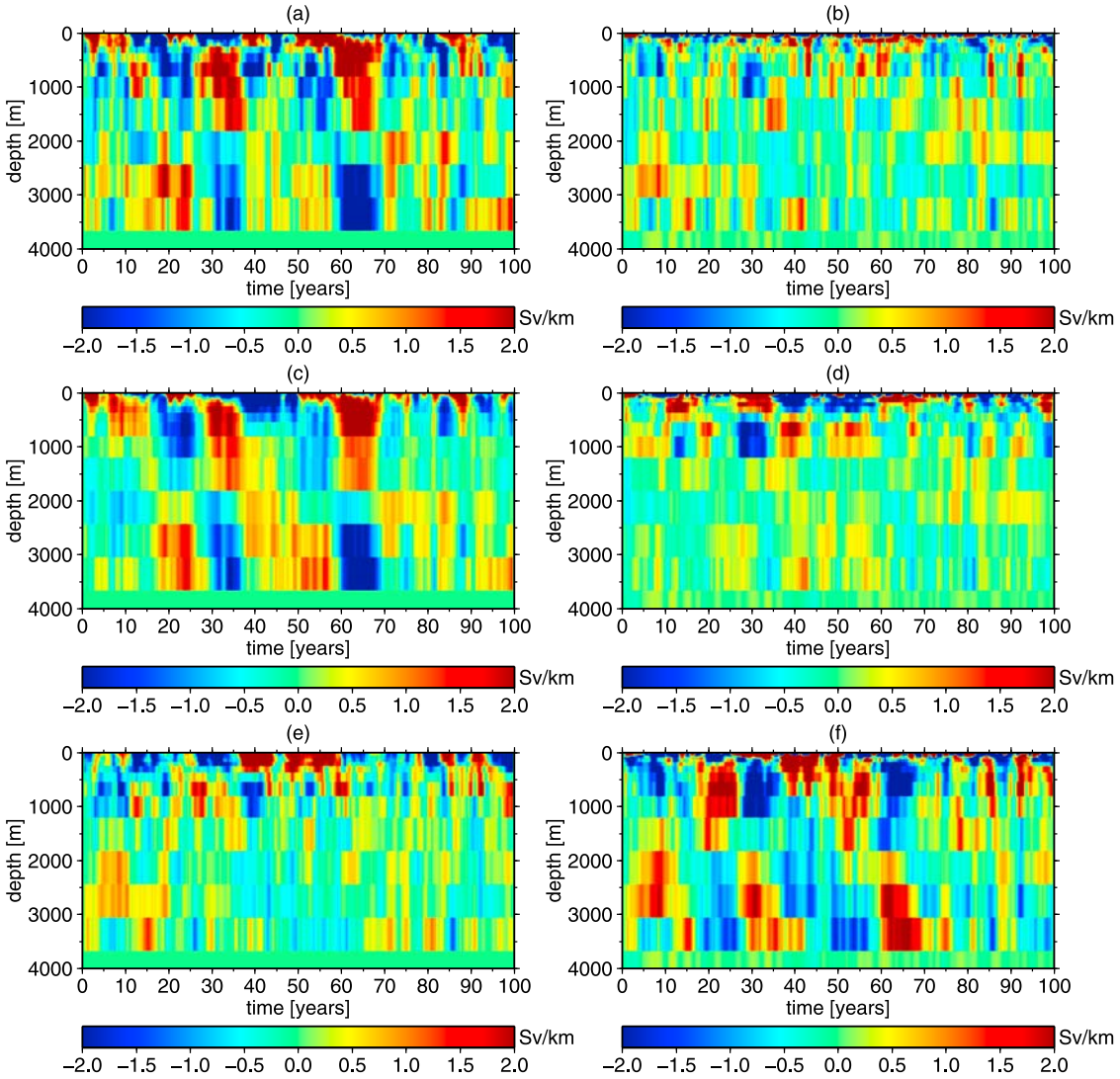

Figure 3. Testing the geostrophic calculation of the zonally integrated meridional transport variability at 50°N in HadCM3. (a) The meridional transport computed using pressure from both the east and west boundaries. (b) The geostrophically computed transport minus the actual transport; (c and d) As in Figures 3a and 3b but using pressure from the western boundary only. (e and f) As in Figures 3a and 3b but using pressure from the eastern boundary only.

[20] Next we consider our ability to determine the transport variability using only pressure from the western boundary. Figures 3c and 3d confirms our earlier result from OCCAM that most of the information required to determine to transport variability, at least in a numerical model, is found on the western boundary. In particular, we find that the two large transport fluctuations are well determined from the western boundary pressure. For the upper layer time series (Figure 4b) the correlation with T_U is 0.94 and the skill (percent of variance accounted for) is 88%. In contrast to the western boundary, very little of the transport variability at 50°N can be recovered using only the eastern boundary pressure (see Figures 3e, 3f, and 4c). When we omit the pressure on this boundary from the geostrophic calculation we do lose part of the meridional transport variability in the upper 1300. But this is a relatively small fraction of the total transport, and the result of the EOF analysis given above suggests that it is quite localized, and not part of the basin-scale coherent mode captured by the western boundary component.

[21] Some insight into these results can be gained from an examination of the fields involved in the geostrophic calculation, namely sea level η, steric height η^s, and, the difference between these two, bottom pressure p^b (when expressed, as it will be throughout this paper, as an equivalent thickness of seawater $h = p^b/g\rho_0$). Considering first the variability on the western boundary, we see the two most prominent fluctuations are clearly manifest in the Hovmöller plot of bottom pressure (Figure 5a). As the transport increases in strength near the end of the second decade, and again near the end of the fifth decade, we see that the bottom pressure goes from positive to negative above the 1800 m isobath and from negative to positive below 1800 m. The relationship is clearly consistent with the geostrophic balance given by equation (1).

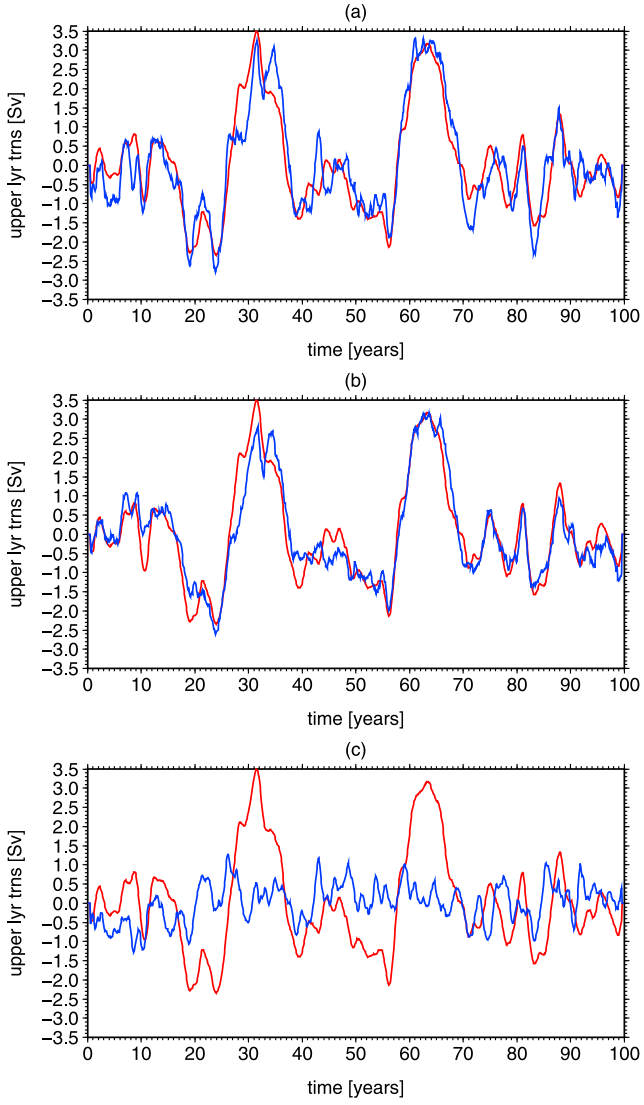

Figure 4. Testing the geostrophic calculation of the zonally integrated meridional transport variability at 50°N in HadCM3. (a) The upper layer (100–1800 m) meridional transport directly calculated (red) and the computed meridional transport using pressure from both the east and west boundaries (blue). (b) As in Figure 4a but using pressure from the western boundary only. (c) As is Figure 4a but using pressure from the eastern boundary only.

[22] Apart from the bottom pressure signal associated with these two large events, there is little additional bottom pressure variability in the western boundary region. This is in stark contrast to the sea level and steric height fields (Figures 5b and 5c), from which bottom pressure is obtained. These fields show much more interannual variability, and, at first sight, do not show a clear relationship with the two large transport fluctuations. Sea level variability is dominated by steric height changes, and the steric variability is not obviously related to the transport strength. This is because much of the steric height variability, particularly toward the higher frequencies, is due to density changes in the upper several hundred meters, whereas the large transport fluctuations depend on changes in density that reach much deeper in the water column.

[23] We now employ the method of compositing to reveal the relationship between each of the three fields and the transport strength as represented by the time series T_U. A high composite of a field F relative to a time series Φ is the mean of F for all times when Φ is greater than some arbitrary threshold value Φ_0. The corresponding low composite is the mean of F for all times when Φ is less than $-\Phi_0$. (Later we refer to high-low composites. These are formed simply by subtracting the low composite from the high composite.) If the time series is of sufficient length, variability unrelated to the process characterized by the reference time series can be averaged out, thus revealing any relationship between the composited field and the process of interest.

[24] Here we use a threshold value of 1 Sv. The high and low composites of the fields over the western boundary are shown in Figures 6a and 6c. The bottom pressure composites (red) confirm the relationship already apparent in the Hovmöller plot: Enhanced transport variability is associated with a shoreward decrease in bottom pressure and an increase on the lower part of the continental slope, which gradually falls to zero toward the deep ocean. The opposite situation occurs when the transport is relatively weak. The steric height field (blue) shows the opposite relationship with the transport strength. A sizeable negative gradient arises in association with a more vigorous transport. In contrast to both the bottom pressure and steric height fields, the sea surface height composites (green) do not develop strong gradients in association with strong or weak states of the transport. This is telling, given that the sea level is, in general, dominated by steric height variability. It suggests that the sea level height gradient produced by the density field is not sustainable, and so there is an adjustment that acts to flatten the sea surface. This point will be significant for our discussion of the dynamics in section 6.

[25] To highlight the different natures of the variability on the eastern and western boundaries, we now consider the high and low composites on the eastern boundary (Figures 6b and 6d). The magnitude of the bottom pressure variability here is generally greater than on the western boundary. Comparison with Figure 3e confirms that this pressure variability corresponds to the shallower component of the meridional transport, lost when we neglect the eastern boundary. However, as discussed previously, this component appears to be localized, and not representative of the more significant, meridionally coherent component of the transport, as revealed by the EOF analysis. As on the western boundary, the pressure variations on the eastern boundary appear to result from an adjustment of the sea surface to eliminate the gradient across the slope that would result from the steric height alone. This is clear in the eastern boundary composites (Figures 6b and 6d), where we see how the sea level is primarily steric east of 14.5°W, but to the west the steric height drops while the sea level flattens out. This difference manifests itself as the observed bottom pressure signal.

[26] Since these eastern boundary composites are based on T_U, which, recall, is well determined from the western boundary pressure, it would appear there is some relationship between the pressure on the two boundaries. Figures 7 and 8 set the variability at the boundaries in the wider context of

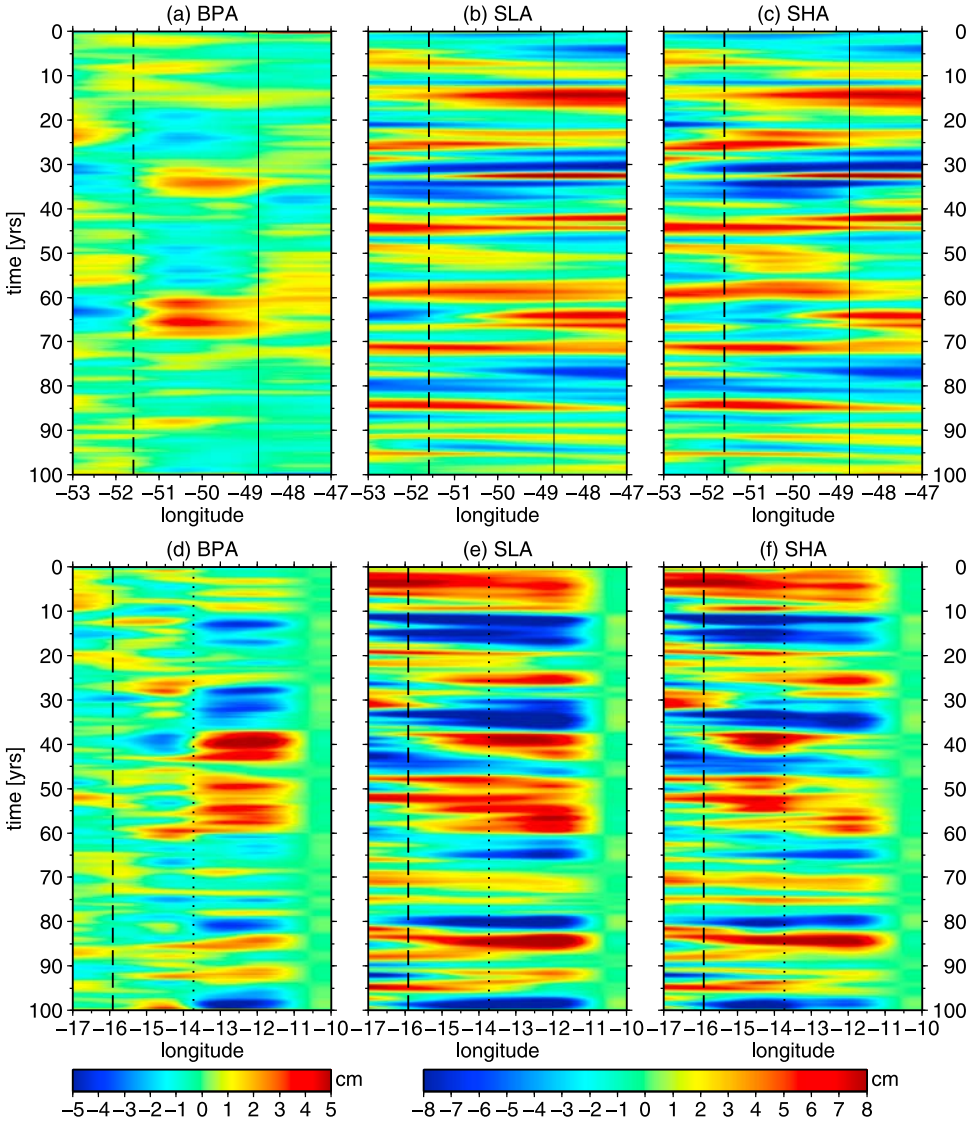

Figure 5. (a–c) HadCM3 interannual bottom pressure, sea level, and steric height variability across the western boundary of the North Atlantic at 50°N. (d–f) As in Figures 5a–5c but for the eastern boundary. In Figures 5a–5c the dashed line represents the position of the 1800 m isobath and the solid line represents the position of the 3000 m isobath. In Figures 5d–5f the dashed line represents the 1800 m isobath and the dotted line represents the 500 m isobath. (Note that due to the coarse resolution of HadCM3 large depth ranges are spanned by a single cell so these positions are only approximate.)

the variability across the entire basin. As expected, the basin wide sea level variability is dominated by steric processes, with bottom pressure generally small in comparison. Unlike sea level, bottom pressure displays a close relationship with the basin topography, with the largest bottom pressure variations occurring at the boundaries, and, to a lesser extent, at other features of the midocean topography. Two characteristics of the steric component of the sea level stand out: First, there is the long period, out of phase behavior between the western and eastern halves of the basin: While the eastern basin is warmer, the western basin is cooler, and vice versa. Second, superimposed on this are apparently eastward propagating anomalies, which appear to cross the basin in approximately four years. Presumably these represent density, primarily temperature, anomalies advected in the mean circulation. Note that we do not see in these plots much evidence for westward propagation such as might arise from Rossby waves. This is to be expected at high latitudes.

[27] The tendency of the basin to be zonally anticorrelated helps explain the apparent relationship between the pressures on the eastern and western boundaries. The density composite (Figure 8d) shows that during times of more vigorous overturning the eastern half of the basin is generally warmer and less dense, while the opposite is true of the western half of the basin. This is consistent with more relatively warm water coming from the south and enhanced cooling in the western subpolar basin. The anomalous density structure explains the form of the steric height and sea level composites (although notice somewhat of an asymmetry between the high and low composites with the east-west difference more pronounced in the case of the high composite.) As will be discussed in section 6, on the western boundary, the positive density

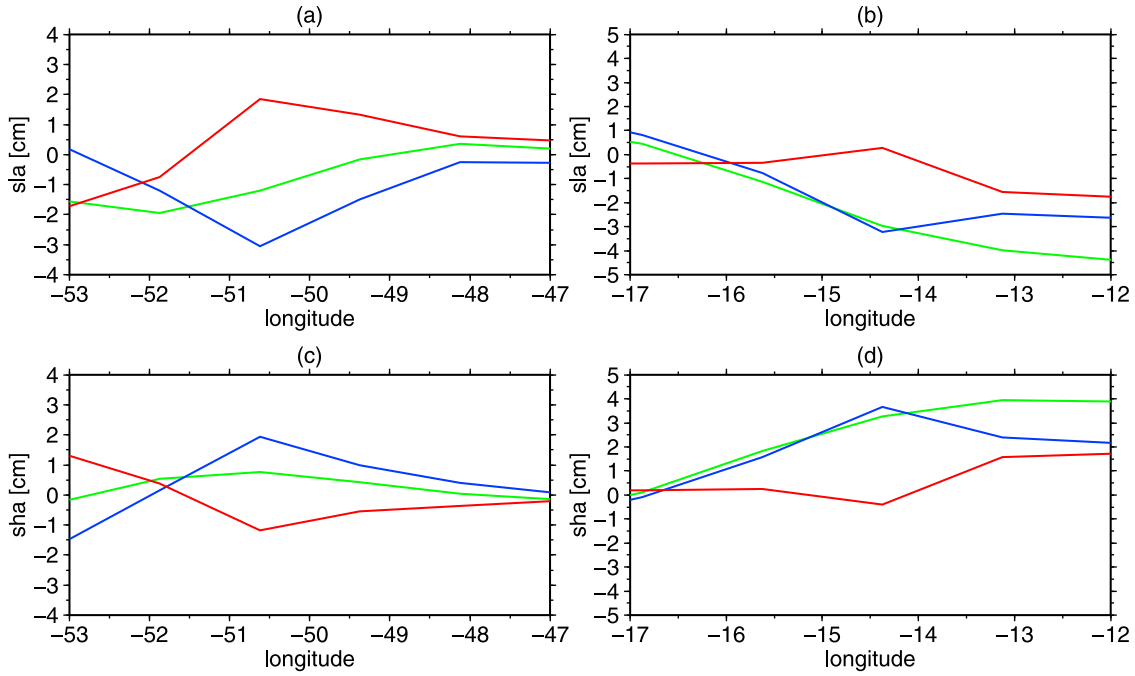

Figure 6. Composites of anomalous bottom pressure (red), sea level (green), and steric height (blue). (a) High composites over the western boundary. (b) High composites over the eastern boundary. (c and d) As for Figures 6a and 6b but for the low composites. Composites (see text for method) are based on the index T_U defined in the text with a threshold value of 1 Sv.

anomaly over the slope leads to a sharp increase in steric height (for the high composite) as the coast is approached, further enhanced by the anomalously warm surface layer. On the eastern boundary the opposite occurs. The steric anomaly (again for the high composite) rapidly decreases toward the coast, although note that in this case the density anomaly does not meet the topography as it does on the west. As a result, there is a smaller change in steric height over the topography, and consequently, a much smaller eastern boundary pressure change and associated transport variation. The pressure variability that does arise is due to the density anomaly that seems trapped near the surface against the eastern boundary and the strong steric height gradient it produces. This is clear in comparing the composites, and is apparent in the Hovmöller diagram by the tendency of the sea level and steric height close to the coast to take the opposite sign to the interior.

5. High-Resolution Model Analysis

[28] Determining an underlying mechanism for the transport variability at 50°N in HadCM3 is somewhat hampered by the low resolution of the model. Toward this end, we now turn to the OCCAM model, which has much higher resolution in both the horizontal and vertical directions. Figure 9 shows, that at 50°N in OCCAM, as in HadCM3, the primary determinant of meridional transport variability is the western boundary pressure. The skill of the transport calculation for the upper and lower layers using only western boundary pressure is 94%. And the standard deviation of the difference between the directly computed time series and the time series calculated from the western boundary pressure is 0.39 Sv for both the upper and lower layer transports. (For the unfiltered case the skill and standard errors scores for the upper layer are 74% and 0.93 Sv and for the lower layer they are 57% and 1.63 Sv. The reasons for this degradation are as for 42°N, as discussed by *Bingham and Hughes* [2008].

[29] Using high-low composites, we find, as in HadCM3, that associated with a strengthened meridional transport at 50°N, there is a significant increase in density, reaching a depth of 2500 m on the western slope (see Figure 10a and an enlargement of the western boundary region in 10b; this enlargement is repeated for each of the rows in Figure 10). The anomalous density increase also extends onto the shelf and into the basin to 35°W, but with much less penetration. A similar composite of temperature (not shown) reveals that this density change is due to cooling of the water column. In contrast, on the eastern boundary there is very little anomalous density signal.

[30] Corresponding to the change in the density field, we also expect to see a change in sea level. High-low composites of sea level, steric height and bottom pressure, are shown in Figures 10c and 10d. The first point to note is that in the interior ocean, east of about 50°W, the sea level variations associated with transport fluctuations are almost entirely due to changes in the density of the water column. The cooling of the water on the western slope results in a drop in steric height here, with a maximum drop of 12 cm near 45°N; the point of maximum penetration of the density signal. The reduction in the magnitude of the positive density anomaly, coupled with the fact that in the interior the increased meridional transport is associated with warming of the upper waters between 35–20°W, results in a steady increase in sea level, reaching a peak of 9 cm at 29°W. Continuing eastward, the first and second drops in sea level clearly correspond to positive density anomalies.

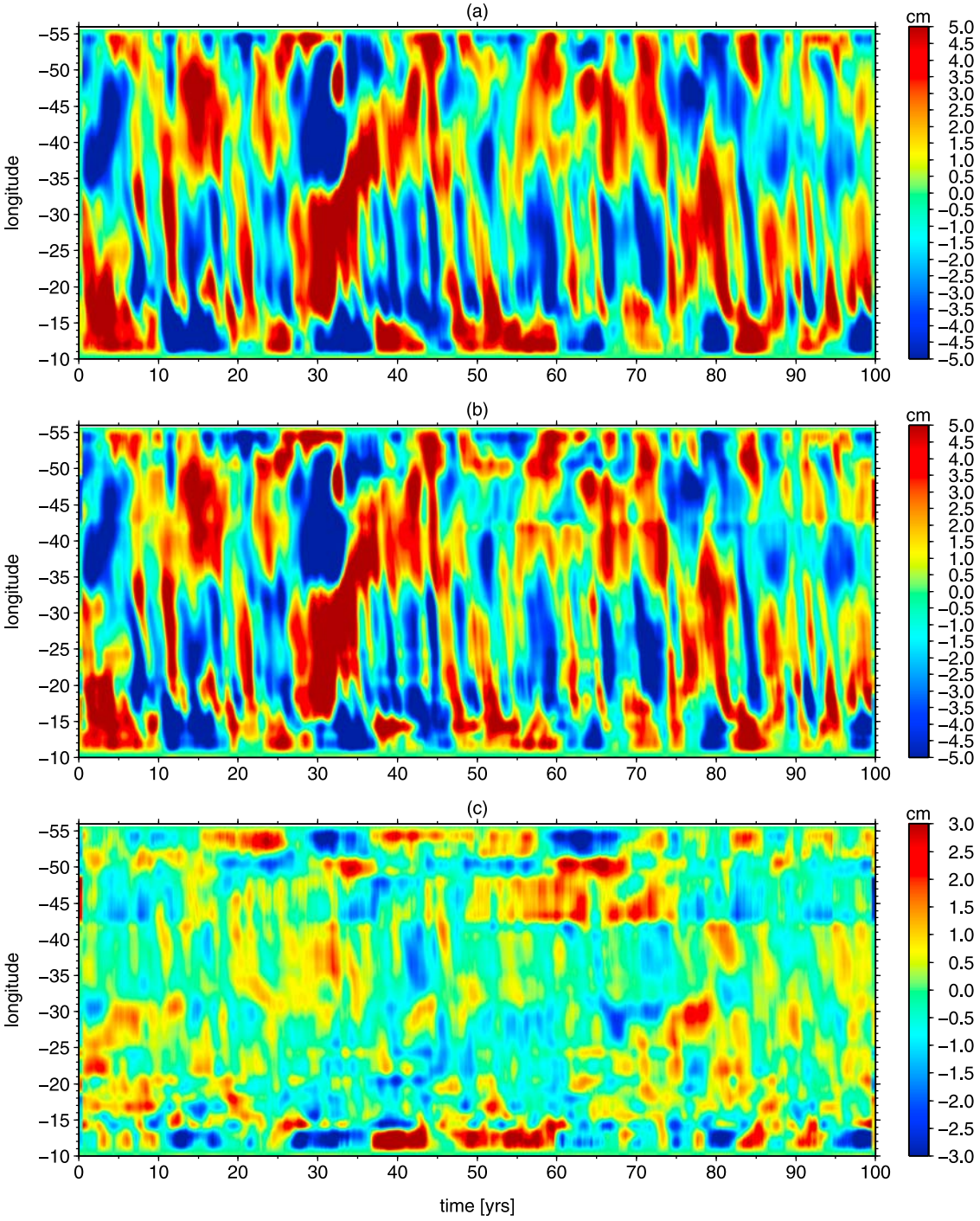

Figure 7. Hovmöller plots showing interannual variability across the North Atlantic basin at 50°N in HadCM3: (a) sea level, (b) steric height, and (c) bottom pressure expressed in equivalent centimeters of water thickness. For each, the zonal mean value has been removed.

[31] In addition to the steric component of sea level, there is also a small barotropic component, which appears at the bottom as a pressure anomaly (Figures 10c and 10d, red). As was found at 42°N [*Bingham and Hughes*, 2008], it is only on the western side of the basin, in this case west of 45°W, where the bottom pressure is significantly different from zero. Over the narrow interval on the western boundary, where bottom pressure determines the meridional transport, we see that the bottom pressure represents a small modification to the steric dominated sea level signal. Initially increasing in magnitude above the upper part of the slope, bottom pressure then falls as depth increases, crossing zero near the 1300 m isobath. On the shelf, the steric height is negligible, and the 3 cm sea level anomaly associated with a positive meridional transport anomaly is almost entirely barotropic.

[32] Clearly, on average, an increase in the meridional transport at 50°N is associated with a strong density signal along the western boundary at 50°N. To see how this density

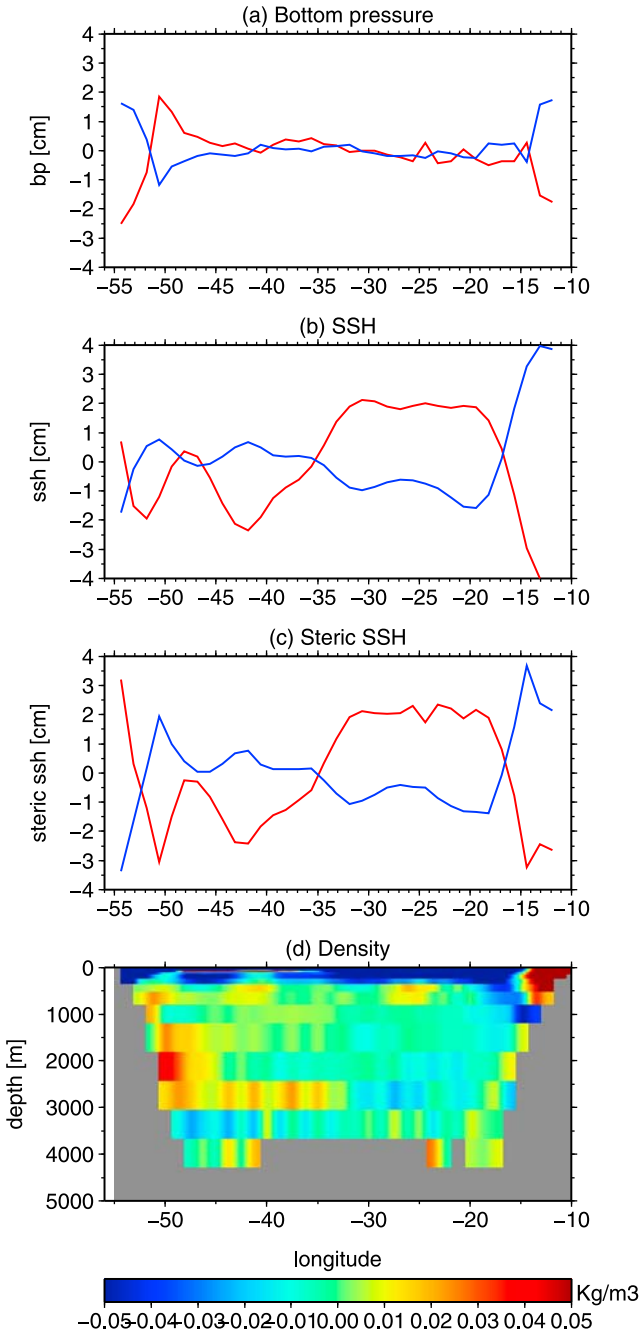

Figure 8. (a–c) High (red) and low (blue) composites of the three fields shown in Figure 7. Composites are based on the index of upper layer transport T_U shown in Figure 2c with a threshold value of 1.0 Sv. (d) The high-low composite of the density in HadCM3 at 50°N.

signal evolves over time, we plot, in Figure 11a, the density profile from 50°N, 48°W. Note that no filtering has been applied to this time series. As Figures 11b and 11c make apparent, the dominance of the low-frequency mode of meridional transport variability at 50°N results from the low-frequency nature of the density signal below the first few hundred meters of the water column and the pressure signal that is associated with it. Associated with the increasing density of the water column, seasonal activity near the surface becomes increasingly vigorous and there is a deepening of the mixed layer.

6. Underlying Dynamics

[33] How do the density changes on the western boundary lead to the observed transport variability? Or, more directly, how do the density changes lead to the observed changes in bottom pressure? From Figure 10b we see that, to a first approximation, the (anomalous) density is horizontally uniform across the slope. A high-low composite of the density profile at 50°N, 48°W is shown in Figure 12a. As a change in density cannot, in itself, produce a change in bottom pressure, we know that, in the absence of other processes, the pressure anomaly at the ocean floor is zero. The pressure profile (expressed as equivalent cm of water thickness) is then given by

$$p(z) = -\rho_0^{-1} \int_{-H}^{z} \rho dz'. \tag{9}$$

The pressure profile obtained from the density profile in Figure 12a is shown in Figure 12b. We see that the increased density of the water column leads to a decrease in pressure at each depth in the water column. The anomalous pressure decreases in magnitude from 11.5 cm at the surface to zero at the bottom. The anomalous pressure near the surface is, of course, the change in steric height, seen clearly in Figure 10d, resulting from the increased density. Note that the pressure profile is nearly linear. This is because the vertical change in

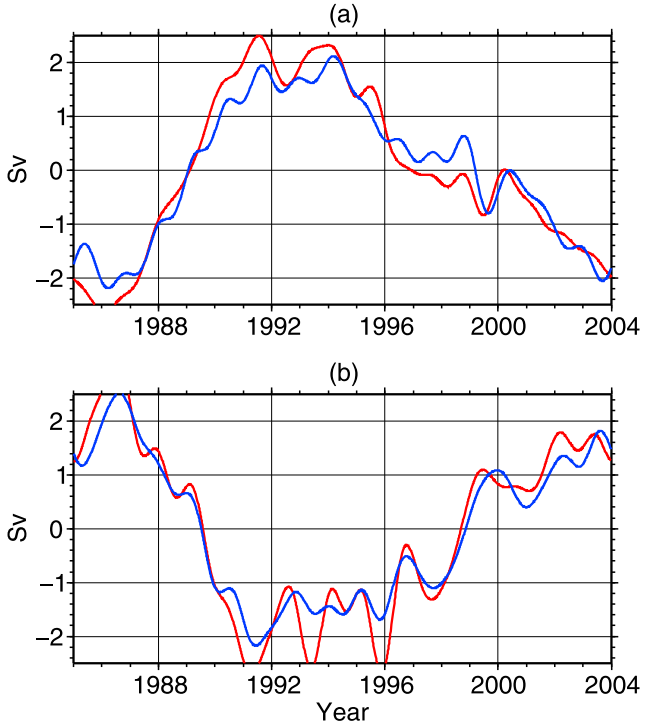

Figure 9. Analysis of 50°N in OCCAM. (a) The low-frequency meridional transport variability integrated over 100–1000 m calculated directly (red) and determined using bottom pressure on the western boundary (blue). (b) As in Figure 9a but for the 1000–3000 m depth range.

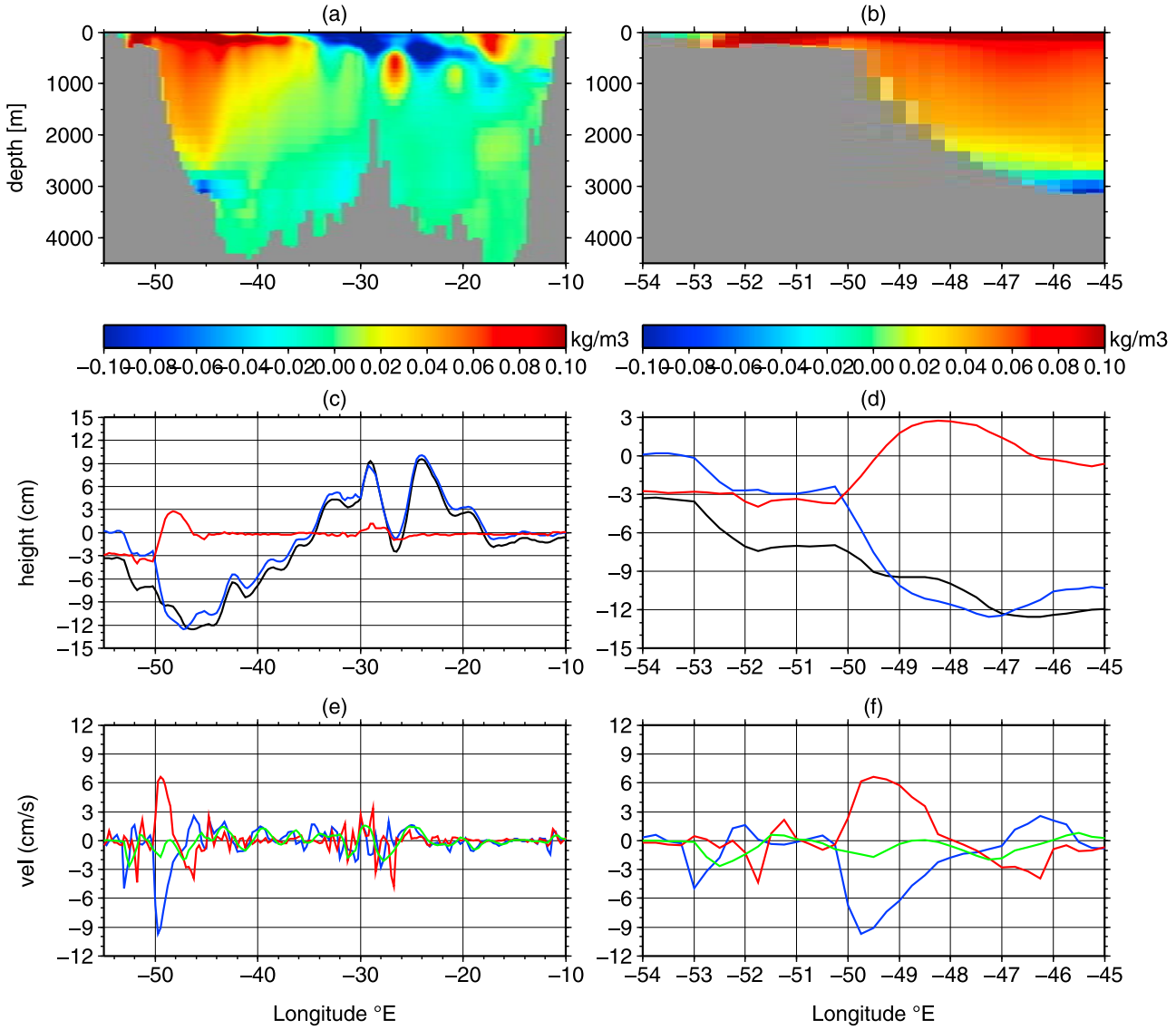

Figure 10. Analysis of 50°N in OCCAM. (a) The difference between the high and low composites of density at 50°N. (c) The difference between the high and low composites of sea level (black), steric height (blue), and bottom pressure (red) at 50°N. (e) The barotropic meridional velocity implied by the density composite (blue) and bottom pressure (red) shown in Figure 10a. These are the second and first term of RHS of equation (17). The actual high-low composite of barotropic meridional velocity (green). (b, d, and f) As in Figures 10a, 10c, and 10e but zooming in on continental slope. Composites based on the upper layer transport time series with a threshold value of 0 Sv.

density is relatively small down to about 2500 m. In other words, the vertical structure of the density anomaly is not important, and a similar pressure profile could be obtained, to first order, from a density anomaly constant in depth. We will use this simplification in our calculation below.

[34] To clarify our thinking regarding the relationship between bottom pressure and density changes on sloping topography, we start by considering an illustrative, highly idealized example. Consider a fluid of uniform density in a rectangular channel (nonrotating) with a linearly sloping bottom, such that it has the cross section shown in Figure 13. The pressure is simply given by $p(z) = -g\rho z$, and the bottom pressure is given by $p^b = g\rho H$, where $H(x)$ is the depth. (For this example, pressure and density are absolute, rather than departures from time-means.) Now consider what happens when the fluid is uniformly cooled such that its density is uniformly increased by $\Delta\rho$. We know that the surface height will change by some amount $h(x)$, but the bottom pressure will not change. Hence $\rho H = (\rho + \Delta\rho)(H + h)$, which gives

$$h = -\frac{\Delta\rho}{\rho + \Delta\rho} H \approx -\frac{\Delta\rho}{\rho} H. \tag{10}$$

Given that the change in height is proportional to the initial water depth, the surface height will fall by more on the right-

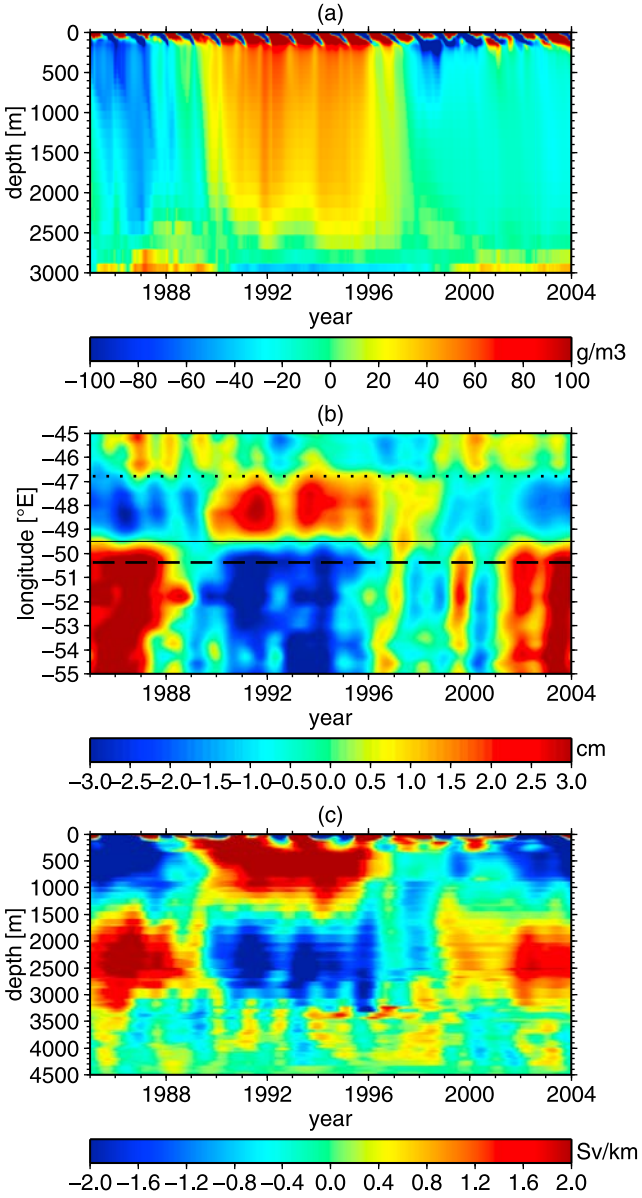

Figure 11. (a) A profile of density taken from the water column on the western slope at 50°N, 48°W. (b) The low-frequency bottom pressure variability on the western boundary. Contours mark depths 340 (dashed), 1300 (solid), and 3000 (dotted) m. (c) The low-frequency zonally integrated meridional transport at 50°N.

hand side (RHS) of the channel than it does on the left-hand side (LHS) as illustrated by the dotted line in Figure 13. In the absence of balancing forces, this situation is, of course, unstable, and fluid will flow from left to right so that the surface is horizontal and there is a zero horizontal pressure gradient (dashed line in Figure 13). While in the cooling phase the mass of each water column was unchanged, in the subsequent equalization phase mass is lost from the left half of the channel and gained by the right half. Hence, there is a change in bottom pressure, with the pressure anomaly increasing, linearly from some value $-\Delta p^b$ on the LHS to Δp^b on the RHS. The bottom pressure change is simply proportional to the change in surface height during the equalization phase

$$\Delta p^b = g\rho_0(h_A - (h_A + h_B)/2) = g\rho_0(h_A - h_B)/2. \tag{11}$$

In reality, of course, the two phases are concurrent and cannot be separated.

[35] Naively applying the above analysis to the situation at 50°N represented in Figure 10d, with side A placed at 50°W and side B at 48°W, we have, from the steric height composite (blue), $h_A = -3$ cm and $h_B = -12$ cm, which gives $\Delta p^b =$ 4.5 cm (when expressed as a water thickness). Thus, our very simple model predicts that given the observed changes in steric height, the western boundary pressure anomaly should grow linearly from −4.5 cm on the shelf edge to 4.5 cm at 2300 m. Surprisingly, given the simplifications and assumptions made (density uniform in x and z, linear bottom slope, artificial eastern boundary, neglecting rotation and other physics) this value is close to the actual value of ±3 cm seen in Figure 10d (red). There is also some indication of the expected flattening of the sea level, which is even more apparent in the HadCM3 composites of sea level (see Figures 6a and 6c).

[36] We shall now put the above simplified model on a more secure theoretical foundation. In geostrophic balance, the meridional component of the depth-mean (barotropic) flow is given by

$$f_0\rho_0\overline{v} = \frac{1}{H}\int_{-H}^{0} p_x dz. \tag{12}$$

Applying Leibniz's rule allows the righthand integral to be written as

$$\int_{-H}^{0} p_x dz = \frac{\partial}{\partial x}\int_{-H}^{0} p dz - H_x p^b. \tag{13}$$

Substituting into this the following expression for pressure as a function of depth:

$$p(z) = p^b - \int_{-H}^{z} g\rho dz', \tag{14}$$

we obtain

$$\int_{-H}^{0} p_x dz = H\left(p^b\right)_x + P_x, \tag{15}$$

where P is the potential energy of the water column

$$P = \int_{-H}^{0} g\rho z dz. \tag{16}$$

Finally, from the geostrophic balance we see that the barotropic meridional velocity is given by

$$\overline{v} = \frac{1}{f_0\rho_0}\left(\left(p^b\right)_x + P_x/H\right). \tag{17}$$

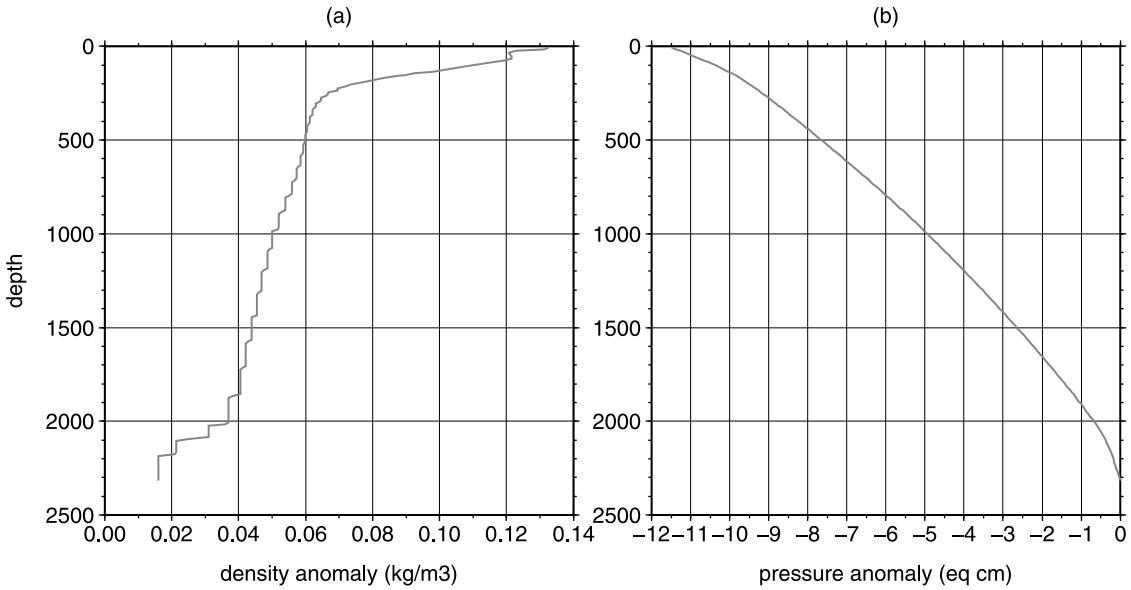

Figure 12. (a) The high-low composite of the profile of anomalous density at 50°N, 48°W. (b) The pressure profile computed from the high-low density profile composite shown in Figure 12a.

So we see that a given potential energy gradient, scaled by depth, will lead to a barotropic velocity (and nonzero, depth-mean transport) to the extent that it is not balanced by an opposing horizontal gradient in bottom pressure. In other words, to say that the horizontal pressure gradient is not balanced by a corresponding geostrophic flow (either because the implied transport is unfeasibly large, or because we are considering a nonrotating scenario, as in the simplified example above) is to say that the potential energy gradient (scaled by depth) is balanced by the horizontal (and therefore depth) gradient in bottom pressure. A barotropic adjustment occurs to limit the barotropic velocity that would otherwise arise from the anomalous density field.

[37] For a homogeneous density anomaly, as just assumed, it is straightforward to show that the RHS of (17) reduces to $g\eta_x/f_0$. So no balancing geostrophic velocity implies a zero surface height gradient, as we have seen occurs for the simple nonrotating channel. Even though the simple analysis above gave a reasonable answer when applied to the OCCAM composite fields (indicating a somewhat homogeneous density field over the slope), the density anomaly clearly varies both vertically and laterally, and so the surface gradient resulting

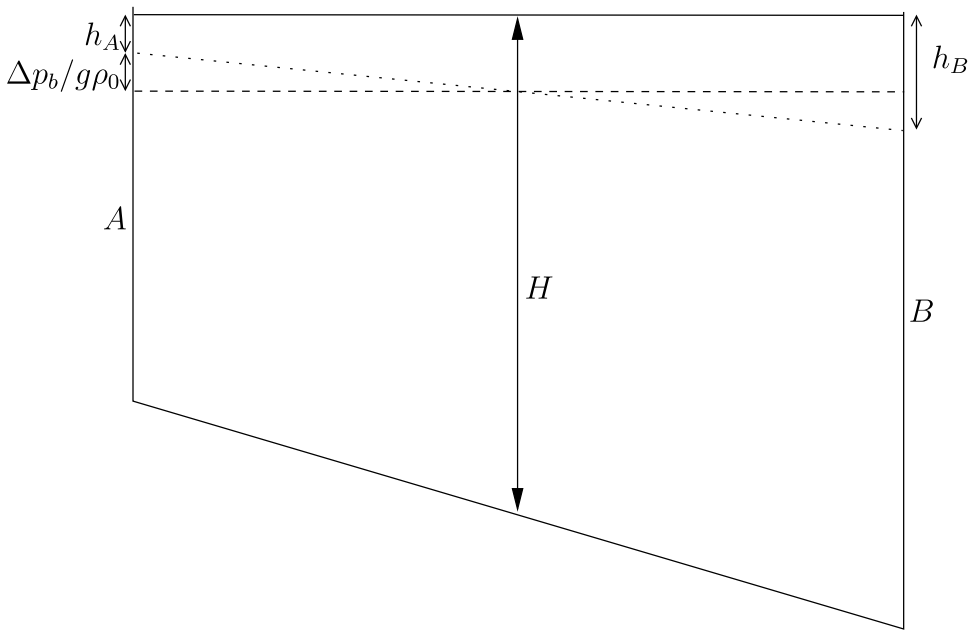

Figure 13. Cross section through a rectangular basin with sloping bottom. Solid line is water level before cooling. Dashed line is the water level after cooling. Dotted line is the intermediate water level due to cooling but before equilibrium.

from a barotropic adjustment will not, in general, be exactly zero. Also the barotropic velocity may not be exactly zero.

[38] However, that the bottom pressure is indeed a *local* barotropic balancing response to the pressure gradients implied by the density field over a sloping topography is clearly demonstrated in Figures 10e and 10f. On the western slope, the southward barotropic velocity implied by the density field (red), given by the second term of the RHS of (17), is largely balanced by a northward barotropic velocity (blue) given by the first term of the RHS of (17). And, as expected, the actual barotropic velocity over the slope (green) is close to zero.

7. Discussion and Conclusions

[39] The zonally integrated transport at a particular latitude and depth is related through geostrophy to the difference in pressure between the east and west boundaries. In this paper we have sought to understand how these pressure differences arise. In the first instance, our analysis of HadCM3 confirms our earlier result from OCCAM [*Bingham and Hughes*, 2008] that the interannual meridional transport variability at latitudes north of 40°N is primarily determined by the bottom pressure on the western boundary. This suggests that this is a feature of ocean models in general. Statistical analysis links this relationship between bottom pressure and meridional transport with changes in density on the western continental slope. Yet, the mechanism by which density changes can lead to variations in pressure is not immediately obvious. With the aid of a highly idealized conceptual model we have shown how a uniform density change in a body of water in a channel with a sloping bottom can lead to a change in bottom pressure through the restoration of the equilibrium condition of a zero horizontal pressure gradient; The initial pressure gradients arising because of the proportional relationship between change in surface height and initial water depth. Finally, we showed that for a more realistic situation this simplified model can be theoretically encapsulated as a balance between the barotropic meridional velocity, the zonal derivative of the potential energy change of the water column (scaled by water depth), and the zonal derivative of the bottom pressure. On the western boundary, the strong density anomaly combines with the steep slope to amplify the potential energy term, which is primarily balanced by the bottom pressure gradient because the implied barotropic velocity is not possible.

[40] We have seen that the relationship between density and the bottom pressure ensures that the barotropic velocity over the slope due to variations in the density field is small (of course, wind induced barotropic transports are a different matter). One can see that in the midocean a density anomaly does not result in net transport. It is only where the density anomaly meets the topography that a net transport can arise. Therefore, the only alternative to a bottom pressure adjustment to ensure mass conservation would be an opposing density anomaly meeting the eastern boundary. While this is possible, there is no underlying dynamical constraint to ensure it. Therefore, in general, it will not be the case. Thus, we see that the bottom pressure anomaly must arise to ensure mass conservation.

[41] As with all modeling studies, one can question the realism of physical processes hypothesized on their basis. The fact that the same mechanism appears in two independent models suggests that the result is general to ocean models. However, one may still ask whether transport variability in models is a realistic representation of what happens in the real ocean. Perhaps the transport variability in the ocean has quite different characteristics and is produced by entirely different means. As discussed below, this question can only be definitively settled with observations, although, in reality, their sparseness can still leave interpretations open to question. That said, sufficient observations exist to examine the realism of one of the key components of our proposed mechanism, namely the density variations on the western boundary.

[42] We have shown that the proximate cause of transport variability in the models is the strong density changes that occur over the western slope. It is appropriate to ask, therefore, whether such changes are realistic, and also whether the lack of such changes on the eastern boundary is realistic. Dealing first with the latter point, it is not unreasonable to suppose that, at high latitudes, density variations with significant depth penetration on the eastern boundary are small in comparison with those on the western boundary, since this where deep water is either formed or soon transported to by the deep western boundary current. Comprehensive observations of the hydrographic structure of the western subpolar North Atlantic have been published by *Yashayaev* [2007]. Comparing his Figure 5 with the anomalous density profile from OCCAM (see Figure 11) shows that both the amplitude of the density variation, and the depth to which the cold density anomaly penetrates, are not unrealistic. Since these factors are critical to the magnitude and form of the pressure anomaly that drives the transport variability in our hypothesis, the observations from the Labrador Sea lend support to our proposed mechanism for transport variability. It is also worth noting that the temporal evolution of the density field in OCCAM, particularly the increasing density anomaly from the early to mid-1990s, follows quite closely that of the observations. Given that *Yashayaev* [2007] and others have linked this to the NAO, the similarity indicates that OCCAM goes some way to a realistic representation of subpolar ocean's response to the prevailing atmospheric conditions.

[43] A critical factor in our proposed mechanism is the interaction of the density field with the sloping topography. Perhaps the limited resolution of the models used influences our results. One possibility is that the modeled anomalous density field is more homogeneous than is the case in reality. However, it is probably reasonable to assume that variations in the density field, particularly at interannual time scales, are large relative to the width of the continental slope. This is particularly true if, as appears to be the case from both tide gauges and altimetry, the slope acts to suppress eddy variability [*Unal and Ghil*, 1995; *Bingham and Hughes*, 2009].

[44] Although our hypothesised mechanism for transport variability depends on the interaction of density with topography, it should not be confused with JEBAR (Joint effect of baroclinicity and topography) introduced by *Sarkisyan and Invanov* [1971]. While this may play some role in the dynamics of this region, it does not impact on our considerations, since, by definition, the transport is purely along geostrophic contours.

[45] The focus of this study has been on an understanding of the geostrophic dynamics of transport variability. Yet, it clearly has implications for how we should monitor the MOC. First, our results indicate that subpolar latitudes are less affected by localized, higher-frequency variability that potentially afflicts lower latitudes. Therefore, compared with the transport variability observed at subtropical latitudes [e.g., *Cunningham et al.*, 2007], the transport variability at subpolar latitudes *may* give a clearer picture of any low-frequency, meridionally coherent variability, which is perhaps nearer to what is intended by the phrase "MOC variability". Second, in confirmation of our earlier results [*Bingham and Hughes*, 2008], we have shown that at subpolar latitudes transport variability can largely be determined from observations from the western boundary. Finally, our results suggest that the transport variability can be recovered from observations of the density field alone. Bottom pressure is not required. This is potentially of great benefit because the tendency of bottom pressure recorders to drift limits their usefulness for long-term monitoring.

[46] In apparent contradiction to our earlier work with OCCAM [*Bingham and Hughes*, 2009], in HadCM3 we do not find a strong relationship between coastal sea level and the strength of the meridional transport. In OCCAM, the steric component of sea level goes to zero at the coast and so the sea level and bottom pressure become identical (Figure 10d) leading to a close relationship between the meridional transport variability and coastal sea level. Figure 10a shows that this is because the density anomaly associated with the transport changes does not penetrate entirely onto the shelf. In contrast, as Figure 7 makes clear, coastal sea level in HadCM3 reflects mainly the steric variability of the interior. This seems to be an issue of resolution. HadCM3 does not adequately resolve the shelf, its width, and perhaps some physical processes such as a shelf currents that act as a barrier to the interior steric signal.

[47] In conclusion, we have described how interannual variations of the zonally integrated transport at 50°N in the North Atlantic can arise primarily from deeply penetrating density anomalies over the western continental slope. Critically, the slope acts to amplify the zonal gradient of potential energy, which is then balanced by an across slope bottom pressure gradient and accompanying changes to the meridional transport, ensuring mass conservation across the basin. While bearing in mind that results from models are never conclusive, our analysis sheds new light on the nature of meridional transport variability in the subpolar North Atlantic, and suggests possible strategies for detecting changes in the meridional overturning circulation.

Appendix A: Sea Level in HadCM3

[48] For a free surface model, sea level η is a prognostic variable, and a readily available model field. However, HadCM3 is a rigid lid model. This complicates matters because η, or rather the pressure exerted by lid $p^s = g\rho_0\eta$, must be diagnosed after the fact from other model output. It can be shown that the surface pressure satisfies the following Poisson equation:

$$\nabla^2 p^s = \rho_0(\nabla \cdot Z - (\mathbf{k} \times \nabla\psi_t)/H), \tag{A1}$$

where Z is the depth-mean baroclinic acceleration (defined shortly), ψ_t is the time derivative of the barotropic stream function (stream function tendency), and H is the water column height [see *Gregory*, 1993]. For HadCM3, equation (A1) is usually solved iteratively using successive over relaxation (SOR). However, we have now established that the solution obtained by this method is inaccurate. While the error is small relative to the range of the variations in sea level, it becomes apparent when we difference the computed sea level from the steric height (computed directly from the density field) to obtain bottom pressure. Because bottom pressure represents a small deviation from the steric dominated sea level variations, particularly over the open ocean and for interannual time scales, its calculation is sensitive to small relative errors in the sea level solutions. In turn, errors in pressure will propagate into the geostrophic calculation of meridional transport. (This is how we found the SOR-calculated rigid lid pressure to be inaccurate.) Fortunately, it is possible to determine the zonal variations in the surface pressure at any particular latitude more directly. And, since we do not require absolute sea level for the geostrophic meridional transport calculation, zonal variations are sufficient.

[49] To derive the required sea level differences, we start by using the hydrostatic balance to substitute for p in the zonal component of the momentum equation (on the beta plane). This allows us to write

$$u_t = u_t' - p_x^s/\rho_0, \tag{A2}$$

where the x subscript denotes zonal differentiation (similarly, below, the y subscript denotes meridional differentiation). In this expression u_t' refers to the baroclinic component of the acceleration and is given by

$$u_t' = -\mathbf{u} \cdot \nabla\mathbf{u} + fv - \frac{g}{\rho_0}\int_z^0 \rho dz' + F^u, \tag{A3}$$

where v is the meridional component of the velocity $\mathbf{u}$, f is the Coriolis parameter and F^u is the zonal component of friction. The acceleration can be written as $u = \hat{u} + \overline{u}$ where $\overline{u}$ is the depth average velocity defined by

$$\overline{u} = \frac{1}{H}\int_{-H}^0 u dz. \tag{A4}$$

If follows that $p_x^s/\rho_0 = u_t' - u_t = u_t' - \overline{u}_t - \hat{u}_t$. However, $\hat{u}_t = u_t' - \overline{u}_t'$ since $\overline{p^s} = p^s$. Hence

$$p_x^s/\rho_0 = \overline{u}_t' - \overline{u}_t. \tag{A5}$$

Since, under the rigid lid approximation, the depth integrated flow is nondivergent we have

$$(H\overline{u})_x + (H\overline{u})_y = 0. \tag{A6}$$

So we can define a stream function such that $H\overline{u} = -\psi_y$. Finally, therefore, we can write

$$p_x^s/\rho_0 = \overline{u}_t' - \frac{1}{H}(\psi_y)_t. \tag{A7}$$

From here, the Poisson equation can be derived by combining the equation with a similar equation for the v component of the momentum equation cross differentiation [e.g., *Bryan*, 1997]. However equation (A7) is sufficient for our needs.

[50] Assuming that on the eastern boundary where $x = x_E$ we have $p^s = p^s_E = \rho_0 \eta_E$. Integrating equation (A7) west from the eastern boundary, and using $p_s = g\rho_0\eta$, then yields an equation for sea level relative to the value on the eastern boundary

$$\eta(x) = -\frac{1}{g}\int_{x_E}^{x}\left(\overline{u}'_t - \frac{1}{H}\left(\psi_y\right)_t\right)dx' + \eta_E. \qquad \text{(A8)}$$

Of course, the value on the eastern boundary η_E remains undetermined. However, since equation (8) involves only relative values of η_e and η_w, it is clear that this is not a problem for the determination of the depth-dependent components of the transport, or, importantly in the context of our analysis, for separating the eastern and western boundary components of the meridional transport.

[51] **Acknowledgments.** This work was funded by grants from the UK Natural Environment Research Council. We thank Andrew Coward and Beverly de Cuevas from the National Oceanographic Centre, Southampton, for their efforts in making the OCCAM model data available. We are grateful for the efforts of two anonymous reviewers whose comments helped us improve the original manuscript.

References

Bingham, R. J., and C. W. Hughes (2008), Determining North Atlantic meridional transport variability from pressure on the western boundary: A model investigation, *J. Geophys. Res.*, *113*, C09008, doi:10.1029/2007JC004679.

Bingham, R. J., and C. W. Hughes (2009), Signature of the Atlantic meridional overturning circulation in sea level along the east coast of North America, *Geophys. Res. Lett.*, *36*, L02603, doi:10.1029/2008GL036215.

Bingham, R. J., C. W. Hughes, V. Roussenov, and R. G. Williams (2007), Meridional coherence of the North Atlantic meridional overturning circulation, *Geophys. Res. Lett.*, *34*, L23606, doi:10.1029/2007GL031731.

Bryan, F. (1997), The axial angular momentum balance of a global ocean general circulation model, *Dyn. Atmos. Ocean.*, *25*(3), 191–216.

Cabanes, C., T. Lee, and L.-L. Fu (2008), Mechanisms of interannual variations of the meridional overturning circulation of the North Atlantic ocean, *J. Phys. Oceanogr.*, *38*(2), 467–480, doi:10.1175/2007JPO3726.1.

Cheng, W., R. Bleck, and C. Rooth (2004), Multidecadal thermohaline variability in an ocean-atmosphere general circulation model, *Clim. Dyn.*, *22*(6), 573–590, doi:10.1007/s00382-004-0400-6.

Cooper, C., and C. Gordon (2002), North Atlantic oceanic decadal variability in the Hadley Centre coupled model, *J. Clim.*, *15*(1), 45–72.

Coward, A., and B. de Cuevas (2005), The OCCAM 66 level model: Physics, initial conditions and external forcing, *Sch. Ocean Earth Sci. Int. Rep. 99*, 58 pp., Natl. Oceanogr. Cent., Southampton, U.K. (Available at http://www.noc.soton.ac.uk/JRD/OCCAM/OCCAM-p25k66-run202.pdf.)

Cunningham, S. A., et al. (2007), Temporal variability of the Atlantic meridional overturning circulation at 26.5°N, *Science*, *317*(5840), 935–938, doi:10.1126/science.1141304.

Curry, R. G., and M. S. McCartney (2001), Ocean gyre circulation changes associated with the North Atlantic Oscillation, *J. Phys. Oceanogr.*, *31*(12), 3374–3400.

Deshayes, J., and C. Frankignoul (2008), Simulated variability of the circulation in the North Atlantic from 1953 to 2003, *J. Clim.*, *21*(19), 4919–4933, doi:10.1175/2008JCLI1882.1.

Eden, C., and R. J. Greatbatch (2003), A damped decadal oscillation in the North Atlantic climate system, *J. Clim.*, *16*(24), 4043–4060.

Eden, C., and T. Jung (2001), North Atlantic interdecadal variability: Oceanic response to the North Atlantic Oscillation (1865–1997), *J. Clim.*, *14*(5), 676–691.

Eden, C., and J. Willebrand (2001), Mechanism of interannual to decadal variability of the North Atlantic circulation, *J. Clim.*, *14*(10), 2266–2280.

Esselborn, S. (2001), Sea surface height changes in the North Atlantic ocean related to the North Atlantic Oscillation, *Geophys. Res. Lett.*, *28*(18), 3473–3476, doi:10.1029/2001GL012863.

Ganachaud, A., and C. Wunsch (2003), Large-scale ocean heat and freshwater transports during the World Ocean Circulation Experiment, *J. Clim.*, *16*(4), 696–705.

Gerdes, R., and C. Köberle (1995), On the influence of DSOW in a numerical model of the North Atlantic general circulation, *J. Phys. Oceanogr.*, *25*(11), 2624–2642.

Gordon, C., C. Cooper, C. Senior, H. Banks, J. Gregory, T. Johns, J. Mitchell, and R. Wood (2000), The simulation of SST, sea ice extents and ocean heat transports in a version of the Hadley Centre coupled model without flux adjustments, *Clim. Dyn.*, *16*, 147–168.

Gregory, J. M. (1993), Sea level changes under increasing atmospheric CO_2 in a transient coupled ocean-atmosphere GCM experiment, *J. Clim.*, *6*(12), 2247–2262.

Guemas, V., and D. Salas-Mélia (2008), Simulation of the Atlantic meridional overturning circulation in an atmosphere-ocean global coupled model. Part I: A mechanism governing the variability of ocean convection in a preindustrial experiment, *Clim. Dyn.*, *31*(1), 29–48.

Hakkinen, S. (2001), Variability in sea surface height: A qualitative measure for the meridional overturning in the North Atlantic, *J. Geophys. Res.*, *106*(C7), 13,837–13,848.

Johnson, H. L., and D. P. Marshall (2002), A theory for the surface Atlantic response to thermohaline variability, *J Phys. Oceanogr.*, *32*(4), 1121–1132.

Kawase, M. (1987), Establishment of deep ocean circulation driven by deep-water production, *J. Phys. Oceanogr.*, *17*(12), 2294–2317.

Köhl, A., and D. Stammer (2008), Variability of the meridional overturning in the North Atlantic from the 50-year GECCO state estimation, *J. Phys. Oceanogr.*, *38*(9), 1913–1930, doi:10.1175/2008JPO3775.1.

Koltermann, K., A. Sokov, V. Tereschenkov, S. Dobroliubov, K. Lorbacher, and A. Sy (1999), Decadal changes in the thermohaline circulation of the North Atlantic, *Deep Sea Res. Part II*, *46*(1–2), 109–138.

Kuhlbrodt, T., A. Griesel, M. Montoya, A. Levermann, M. Hofmann, and S. Rahmstorf (2007), On the driving processes of the Atlantic meridional overturning circulation, *Rev. Geophys.*, *45*, RG2001, doi:10.1029/2004RG000166.

Latif, M., C. Böning, J. Willebrand, A. Biastoch, J. Dengg, N. Keenlyside, U. Schweckendiek, and G. Madec (2006), Is the thermohaline circulation changing?, *J. Clim.*, *19*(18), 4631–4637, doi:10.1175/JCLI3876.1.

Levitus, S., and T. Boyer (1994), *World Ocean Atlas 1994*, vol. 4, *Temperature*, *NOAA ATLAS NESDIS*, vol. 4, 129 pp., NOAA, Silver Spring, Md.

Levitus, S., R. Burgett, and T. Boyer (1994), *World Ocean Atlas 1994*, vol. 3, *Salinity*, *NOAA ATLAS NESDIS*, vol. 3, 111 pp., NOAA, Silver Spring, Md.

Manabe, S., and R. J. Stouffer (1999), The role of thermohaline circulation in climate, *Tellus Ser. A*, *51*(1), 91–109.

Marsh, R. (2000), Recent variability of the North Atlantic thermohaline circulation inferred from surface heat and freshwater fluxes, *J. Clim.*, *13*(18), 3239–3260.

Mauritzen, C., and S. Hakkinen (1999), On the relationship between dense water formation and the "Meridional Overturning Cell" in the North Atlantic ocean, *Deep Sea Res. Part I*, *46*(5), 877–894.

McManus, J. F., R. Francois, J. M. Gherardi, L. D. Keigwin, and S. Brown-Leger (2004), Collapse and rapid resumption of Atlantic meridional circulation linked to deglacial climate changes, *Nature*, *428*(6985), 834–837, doi:10.1038/nature02494.

Sarkisyan, A. S., and V. F. Invanov (1971), The combined effect of baroclinicity and bottom relief as an important factor in the dynamics of ocean currents, *Ivz. Russ. Acad. Sci. Atmos. Ocean Phys. Engl. Trans.*, *7*, 173–188.

Sime, L. C., D. P. Stevens, K. J. Heywood, and K. I. Oliver (2006), A decomposition of the Atlantic meridional overturning, *J. Phys. Oceanogr.*, *36*(12), 2253–2270, doi:10.1175/JPO2974.1.

Spall, M. A. (2008), Low-frequency interaction between horizontal and overturning gyres in the ocean, *Geophys. Res. Lett.*, *35*, L18614, doi:10.1029/2008GL035206.

Talley, L. D., J. L. Reid, and P. E. Robbins (2003), Data-based meridional overturning stream functions for the global ocean, *J. Clim.*, *16*(19), 3213–3226.

Unal, Y., and M. Ghil (1995), Interannual and interdecadal oscillation patterns in sea level, *Clim. Dyn.*, *11*, 255–278.

Vellinga, M., and R. A. Wood (2002), Global climatic impacts of a collapse of the Atlantic thermohaline circulation, *Clim. Change*, *54*(3), 251–267, doi:10.1023/A:1016168827653.

Wood, R. A., M. Vellinga, and R. Thorpe (2003), Global warming and thermohaline circulation stability, *Philos. Trans. R. Soc. London Ser. A*, *361*(1810), 1961–1975, doi:10.1098/rsta.2003.1245.

Yashayaev, I. (2007), Hydrographic changes in the Labrador sea, 1960–2005, *Prog. Oceanogr.*, *73*(3–4), 242–276, doi:10.1016/j.pocean.2007.04.015.

Zhu, X., and J. Jungclaus (2008), Interdecadal variability of the meridional overturning circulation as an ocean internal mode, *Clim. Dyn.*, *31*(6), 731–741, doi:10.1007/s00382-008-0383-9.

R. J. Bingham, Department of Civil Engineering and Geosciences, Newcastle University, Cassie Bldg., Newcastle upon Tyne NE1 7RU, UK. (r.j.bingham@ncl.ac.uk)

C. W. Hughes, Proudman Oceanographic Laboratory, Joseph Proudman Bldg., 6 Brownlow St., Liverpool L3 5DA, UK.